ACS APPLIED MATERIALS & INTERFACES
Research Article
www.acsami.org

Fine Tuning of Lithographic Masks through Thin Films of PS-*b*-PMMA with Different Molar Mass by Rapid Thermal Processing

Federico Ferrarese Lupi,[‡] Tommaso Jacopo Giammaria,[‡,§] Gabriele Seguini,[‡] Francesco Vita,[#] Oriano Francescangeli,[#] Katia Sparnacci,[§] Diego Antonioli,[§] Valentina Gianotti,[§] Michele Laus,[§] and Michele Perego*[,‡]

[‡]Laboratorio MDM, IMM-CNR, Via C. Olivetti 2, 20864 Agrate Brianza, Italy

[#]Dipartimento di Scienze e Ingegneria della Materia, dell'Ambiente ed Urbanistica and CNISM, Università Politecnica delle Marche, Via Brecce Bianche, 60131 Ancona, Italy

[§]Dipartimento di Scienze e Innovazione Tecnologica (DISIT), Università del Piemonte Orientale "A. Avogadro", INSTM, UdR Alessandria, Viale T. Michel 11, 1512 Alessandria, Italy

ABSTRACT: The self-assembly of asymmetric polystyrene-*b*-poly(methyl methacrylate) (PS-*b*-PMMA) block copolymer based nanoporous thin films over a broad range of molar mass (M_n) between 39 kg·mol^{-1} and 205 kg·mol^{-1} is obtained by means of a simple thermal treatment. In the case of standard thermal treatments, the self-assembly process of block copolymers is hindered at small M_n by thermodynamic limitations and by a large kinetic barrier at high M_n. We demonstrate that a fine tuning of the annealing parameters, performed by a Rapid Thermal Processing (RTP) machine, permits us to overcome those limitations. Cylindrical features are obtained by varying M_n and properly changing the corresponding annealing temperature, while keeping constant the annealing time (900 s), the film thickness (~30 nm), and the PS fraction (~0.7). The morphology, the characteristic dimensions (i.e., the pore diameter d and the pore-to-pore distance L_0), and the order parameter (i.e., the lattice correlation length ξ) of the samples are analyzed by scanning electron microscopy and grazing-incidence small-angle X-ray scattering, obtaining values of d ranging between 12 and 30 nm and L_0 ranging between 24 and 73 nm. The dependence of L_0 as a 0.67 power law of the number of segments places these systems inside the strong segregation limit regime. The experimental results evidence the capability to tailor the self-assembly processes of block copolymers over a wide range of molecular weights by a simple thermal process, fully compatible with the stringent constraints of lithographic applications and industrial manufacturing.

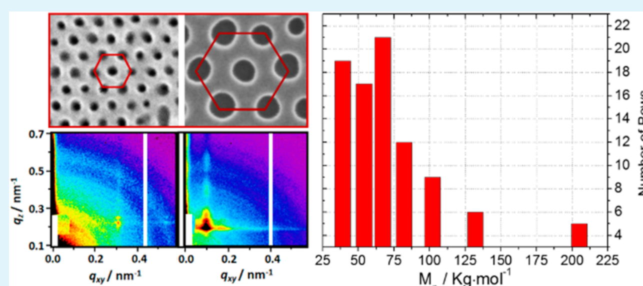

KEYWORDS: *block copolymer, self-assembly, rapid thermal processing, GISAXS analysis, nanopatterning, molecular mass*

INTRODUCTION

Highly immiscible block copolymers (BCPs) have gained increasing interest over the last decade due to their ability to self-assemble into structures featuring periodicities at the nanometric scale. Due to this peculiar characteristic, BCPs appear to be suitable candidates for technologies involving surface patterning to be exploited in a wide range of emerging fields in nanotechnology, such as virus and water filtration,[1−3] organic optoelectronics,[4] anti-reflection coatings,[5,6] and nanolithography.[7−9] Current "top-down" photolithographic procedures are well established and highly optimized, supporting the progressive scaling-down of microelectronics over the last few decades. Nevertheless, inherent physical limitations related to optical diffraction in 193 nm lithography[10] forced microelectronic industries to develop quite complex and expensive procedures, such as double patterning and immersion lithography,[11] in order to achieve the goals of the 32 and 22 nm nodes. A further extension of the photolithographic techniques beyond the 22 nm limit would require the introduction of even more complex and expensive multiple exposure lithographic tools. In this context, non-optical "bottom up" lithographic approaches using self-assembling (SA) materials have been proposed as a complementary process to partially overcome the limitations of current photolithography.[12,13] In this regard, thin films of SA BCPs are of great interest for application in the semiconductor industry, owing to the possibility of integrating these cost-effective lithographic materials with the standard "top-down" processes.[14]

From a general point of view, the morphology of the BCP film, involving lamellae, gyroids, spheres, and cylinders,[15] can be controlled by varying the relative volume fraction f of the two blocks whereas, within each morphology, the structure periodicity can be tuned by varying the BCP molar mass (M_n).

Received: January 15, 2014
Accepted: April 17, 2014
Published: April 17, 2014

 © 2014 American Chemical Society

In this context, several BCPs have been already investigated, such as polystyrene-*b*-polydimethylsiloxane (PS-*b*-PDMS), polystyrene-*b*-poly(methyl methacrylate) (PS-*b*-PMMA), polystyrene-*b*-poly2-vinylpyridine (PS-*b*-P2VP), or polystyrene-*b*-poly(ethylene oxide) (PS-*b*-PEO).

Among these, PS-*b*-PMMA represents a good candidate for integration with current "top down" approaches, because it holds most of the characteristics required by an ideal sub-lithographic patterning material.[16] First of all, PS-*b*-PMMA is soluble in common solvents such as toluene or tetrahydrofuran. Then, the selectivity of the PMMA with respect to acetic acid allows a selective removal of the PMMA phase, thus leading to the fabrication of a PS robust template for the pattern transfer to the substrate. Furthermore, due to the relatively weak interaction energy between the two blocks, both perpendicular and parallel orientation of the nanodomains are easily accessible by properly controlling the surface−polymer interaction[17,18] through the deposition of homopolymer[19] or random copolymer (RCP) thin films.[20,21] The main limitation of PS-*b*-PMMA is the minimum feature size obtainable with this BCP. The minimum achievable size of the periodicity of the polymeric film is dictated by the relatively low energy interaction between the two blocks, which prevents the phase separation in low M_n PS-*b*-PMMA BCPs. On the other side, the low mobility and slow ordering kinetics of the high M_n PS-*b*-PMMA BCPs control the maximum achievable size of the periodicity.

Extremely long annealing times (between 10^2 and 10^3 min) are required to obtain the vertical orientation, which represents the suited orientation for the preparation of a lithographic mask, when the self-assembling process is driven by pure thermal treatments.[22,23] For this reason, alternative or complementary techniques have been investigated including the use of external electric fields during the thermal treatment,[24,25] directional solvent vapor flow,[26,27] shear-induced alignment,[28] and solvent vapor annealing (SVA), eventually in combination with microwave radiation[29] or thermal annealing.[30,31] Nevertheless, the complexity of solvothermal setup and the dependence of the SA process on the experimental parameters of the SVA system (i.e., distance between solvent and sample, solvent vapor composition, absolute chamber pressure, temperature, humidity) result in poor reproducibility of the samples.[32]

Recently, a novel technology, rapid thermal processing (RTP), was employed to control the SA process of BCPs.[33,34] This technique involves the use of the infrared radiation of the RTP apparatus to govern the temperature of the polymeric films. Very high heating and cooling rates can be adopted, thus making it possible to attain high temperature short time thermal cycles. Well organized cylinder morphologies in films of 30 nm of an asymmetric 67 kg mol^{-1} PS-*b*-PMMA were obtained in less than 60 s.[33]

The present work extends the use of RTP to the processing of thin films of cylinder forming PS-*b*-PMMA samples featuring a wide range of molar mass, with M_n comprised between 39 to 205 kg·mol^{-1}. In this context, it is pertinent to observe that whereas for symmetric BCPs the SA process dependence on the M_n has been intensively investigated,[35−37] only few works on this issue are found in the literature for asymmetric PS-*b*-PMMA thin films.[24,38]

EXPERIMENTAL SECTION

Surface Neutralization. Oriented Si(100) substrates with a 100 nm thick thermal SiO_2 layer were used as a support for the BCP deposition. The oxidized substrates (about 1 cm^2 surface) were cleaned with piranha solution (H_2SO_4/H_2O_2 with 3/1 vol. ratio at 80 °C for 40 min) to eliminate any residual organic material and to increase the surface concentration of hydroxyl groups. The samples were then rinsed in H_2O, dried under N_2 flow, cleaned with isopropanol in an ultrasonic bath, and finally dried under N_2 flow. After the cleaning process, a solution of a functional poly(styrene-*r*-methyl methacrylate) (P(S-*r*-MMA)) with styrene fraction 0.62 (M_n = 13.5 kg·mol^{-1} and polydispersity index PDI = 1.26, Polymer Source Inc.) (18.0 mg in 2.0 mL of toluene) was prepared in an ultrasonic bath and then spun on the substrates for 30 s at 3000 rpm. This particular RCP was chosen on the basis of previous results reported in the literature on the vertical orientation of the cylindrical nanodomains obtained on the same BCP.[39,40] In these conditions, a film thickness around 30 nm is obtained. Grafting was obtained by thermally treating the samples[21] in RTP under N_2 atmosphere. The RTP machine is a standard semiconductor manufacturing equipment that employs radiative energy sources (normally halogen lamps) to drive the desired temperature on the sample with extremely high heating rates. In the present experiments the grafting of the RCP was promoted with an annealing process at 250 °C for 600 s with a heating rate of 18 °C/s. The cooling velocity was controlled by changing the N_2 flow rate, resulting in a cooling rate of 10 °C/s. Consequently, the time required to bring the temperature of the sample below the T_g was about 20 s. After the removal of the non-grafted P(S-*r*-MMA), performed with an ultrasonic bath in toluene, the thickness of the grafted RCP layer was ~7 nm.

Block Copolymer Deposition and Self-Assembly. Asymmetric PS-*b*-PMMA BCPs with different molar masses (M_n, styrene volume fraction *f*, and PDI values are listed in Table 1) were purchased from Polymer Source Inc. and used without further purification. The samples having different M_n have been marked with the letter B, standing for Block, and a number representing the corresponding value of molar mass (e.g. B102 corresponds to the BCP with M_n = 102 kg·mol^{-1}). Thermogravimetric analyses (TGA) were performed using a Mettler-Toledo thermobalance mod. TGA/SDTA 851^e LF1100 at a scanning rate of 20 °C·min^{-1} from room temperature up to 600 °C under N_2 flow.

Table 1. Molar Mass (M_n) of the BCP, Molar Mass (M_n *Styrene*) of the Polystyrene Block, Polystyrene Volume Fraction (*f*), and Polydispersity Index (PDI) of All the BCPs

sample	M_n (kg/mol)	M_n *Styrene* (kg/mol)	*f*	PDI
B29	29.4	21.5	0.75537	1.10
B39	39.0	26.8	0.71367	1.07
B54	53.8	37.0	0.71419	1.07
B67	67.1	46.1	0.71353	1.09
B82	82.0	57.0	0.72121	1.07
B102	101.5	68.0	0.69725	1.08
B132	132.0	96.0	0.75159	1.11
B205	205.0	140.0	0.70962	1.16

A solution of the various PS-*b*-PMMA (18.0 mg in 2.0 mL of toluene) was spun for 30 s at 3000 rpm on the grafted RCP. The self-organization of the PS-*b*-PMMA films was induced, by RTP under N_2 flow, heating the samples to the annealing temperature (T_A) at 18 °C s^{-1} and maintaining the samples at T_A for 900 s.

The thickness of the polymeric films was measured by means of an M-200U spectroscopic ellipsometer (J. A. Wollam Co. Inc.) using light radiation from a Xe lamp impinging on the sample at a 70° incidence angle. Films of controlled thickness (~30 nm) were deposited for each PS-*b*-PMMA BCP on the properly neutralized substrates via spin-coating from dilute solutions of PS-*b*-PMMA in toluene (1% w/w) for 30 s at 3000 rpm.

Morphological Analysis. The morphology of the BCPs (in-plane order and orientation with respect to the substrate) was investigated by means of scanning electron microscopy (SEM, Zeiss Supra 40) and grazing-incidence small-angle X-ray scattering (GISAXS). GISAXS was performed at the ID01 beamline of the European Synchrotron Radiation Facility (ESRF, Grenoble, France), using an incident beam energy of 8.0 keV, corresponding to a wavelength $\lambda = 0.155$ nm, and a two-dimensional MAXIPIX fast readout photon-counting pixel detector (four chips, 516 × 516 pixels, pixel size 55 μm), positioned at the end of a vacuum tube. The beam diameter was ∼100 μm and the sample-to-detector distance 0.830 m. Samples and detector were mounted on a high resolution $\theta-2\theta$ goniometer, allowing a fine control of the incidence angle.

In order to enhance the phase contrast in both SEM and GISAXS characterizations, a selective removal of the PMMA component was performed. The degradation of the PMMA and parallel cross-linking of the PS were achieved by exposure to UV radiation (5 mW cm^{-2}, λ = 253.7 nm, 900 s). The PMMA material was subsequently removed through immersion in an acetic acid bath and subsequent rinsing in deionized H_2O. Finally, oxygen plasma treatments were performed to remove the RCP at the bottom of the pores.

■ RESULTS AND DISCUSSION

In general, the deposition and processing of a specific BCP involve the optimization of several parameters including the film thickness as well as the annealing time and temperature. However, the constraints dictated by the successful exploitation of these materials in industrial applications impose certain limits which represent, to some extent, inescapable boundary conditions.

When the ordering process is carried out by conventional thermal treatments in an oven/furnace, the formation of uniform patterns usually requires combining proper optimization of the annealing conditions with fine tuning of the thickness of the BCP film.[16] The thickness to produce a uniform polymeric template over the sample surface decreases as the M_n of the BCP decreases. However, in view of the technological application of the PS-*b*-PMMA scaffold as sacrificial layer for pattern transfer, the thickness of the deposited film has to sustain additive or subtractive strategies for nanostructure fabrication on the underlying substrate. In this regard, the possibility of a nanoporous polymeric film of fixed thickness (∼30 nm) with tunable characteristic lengths (d, L_0) would represent a step towards the simplification of the subsequent lithographic processes.

Even if the effectiveness of annealing times shorter than 60 s has already been demonstrated for relatively small M_n BCPs,[33,34] in this work an annealing time of 900 s was always adopted to afford all the BCPs, irrespective of their specific M_n, enough time to self-organize with a minimum level of order. Moreover, this annealing time allows maintaining the samples in an isothermal condition for a relatively long time at the different investigated temperatures. This prolonged isothermal condition allows minimizing the contribution of the transients on the overall thermal treatment and to effectively investigate the effect of T_A variations on the microphase separation and ordering process. Nevertheless, this annealing time is still much shorter than those adopted for other thermal treatments and definitely fulfills the industrial requirements for manufacturing processes. Consequently, the phase separation and lateral organization of the PS-*b*-PMMA BCPs with different M_n values (from 29.4 kg·mol^{-1} to 205 kg·mol^{-1}) are promoted by changing the annealing temperature T_A in a RTP system. The surface neutralization, all the deposition (i.e., BCP film thickness and type of solvent) and annealing parameters (i.e., annealing time, heating ramp, and N_2 flow) were kept constant.

Once these boundary experimental conditions were defined, the optimization of the SA process mainly relies on the determination of the window of temperatures that can be operated to promote the phase separation and ordering of the BCP with the PMMA blocks arranged into hexagonally packed cylinders oriented perpendicularly to the substrate. The glass transition temperature (T_G) sets the lower limit whereas the upper working temperature is given by the degradation temperature (T_{DEG}) of the PS-*b*-PMMA. The value of the T_G in the bulk phase is known to be $T_G \sim 110$ °C for the PS and $T_G \sim 124$ °C for the PMMA, with a very limited variation ($\Delta T_G \pm 2$ °C) depending on the M_n. On the other hand, the T_{DEG} of the BCPs are known to be significantly affected by the M_n. Accordingly, the thermal stability of each BCP was investigated through TGA analyses. Although the T_G and the T_{DEG} values in thin films are expected to differ from those measured in bulk, the measurement of the aforementioned limits in the bulk phase represents a useful guideline for the optimization of the T_A.

Figure 1a reports collectively the TGA curves, recorded under N_2 flow at the heating rate of 20 °C·min^{-1}, for all the BCPs. In all cases, a sigmoidal shape of the loss curve is observed. As the M_n increases, the loss curves are regularly shifted toward higher temperature values. However, subtle differences can be noticed within the various samples, especially corresponding to the initial stages of the thermal degradation. For the lowest M_n sample (B29), the beginning of the loss curve occurs at the lowest temperature (about 250 °C, Figure 1b), and a single weight loss is observed extending over a wide temperature region. As the molar mass increases, the temperature corresponding to the initial degradation stage increases and the width of the weight loss profile slightly decreases. These differences in the thermal degradation profile probably account for the increasingly more relevant contribution of the end groups in initiating the thermal degradation, as

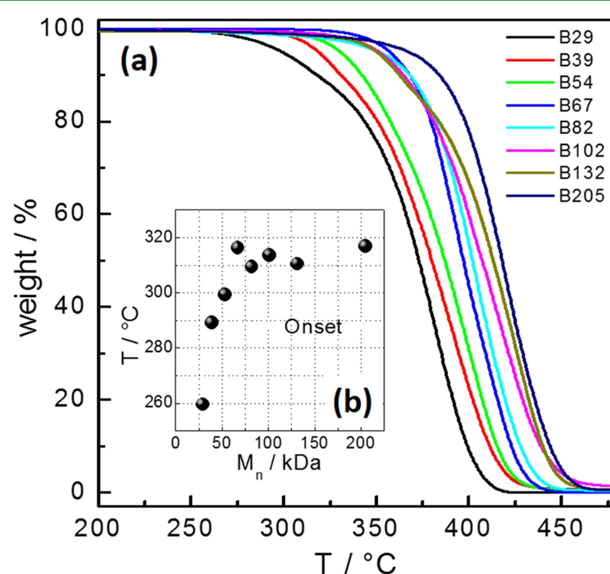

Figure 1. (a) TGA curves at 20 °C·min^{-1} heating rate under N_2 flow for the PS-*b*-PMMA BCPs with different M_n. The inset (b) reports the temperatures corresponding to the onsets of the thermal degradation as a function of BCP M_n.

the average M_n decreases.[41] On the basis of the latter results we set the onset values T_{DEG} of the degradation curves as upper bounds of the working temperature window. The relevant T_{DEG} data as a function of M_n are reported in Figure 1b. The T_{DEG} values initially increase and subsequently level off at high M_n, further supporting the hypothesis of a significant role of the end groups in the thermal degradation process. It is worth noting that the T_{DEG} increase with the M_n leads to a progressive enlargement of the window of accesible temperatures. In turn, the T_{DEG} increase allows the high M_n BCPs to be processed at high temperatures, thus decreasing the melt viscosity and increasing the kinetics of the ordering process.

Morphological Analysis. To establish the optimum T_A range for the SA of each BCP, a systematic SEM analysis of the morphology of the annealed polymeric films was performed in a wide temperature range. Figure 2 shows a series of SEM images for sample B102 as a typical example. At 190 °C, the SA process appears in a preliminary stage (Figure 2a). The phase separation and the perpendicular orientation of the PMMA cylinders are achieved, but the hexagonal order of the cylinders is not completely developed.[42] In contrast, at 230 °C a well-defined hexagonal arrangement of the PMMA cylinders is obtained with a good lateral order (Figure 2b). On further increasing the T_A (250 °C), a number of defects become apparent (Figure 2c), and, finally, the hexagonal pattern completely disappears for T_A higher than 270 °C (Figure 2d). It is worth noting that, under the adopted experimental conditions, the nanometric films do not show any sign of degradation. Therefore, the breakdown of the hexagonal arrangement at $T_A \geq 250$ °C is likely to occur because the T_A approaches the order−disorder transition temperature (T_{ODT}).

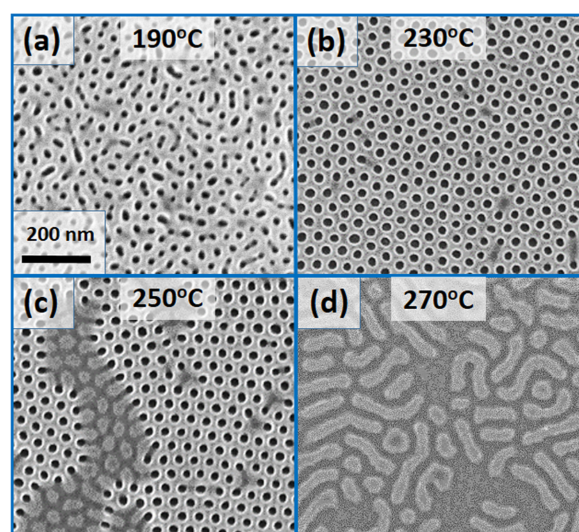

Figure 2. SEM images of sample B102 at four different annealing temperatures: (a) 190 °C, (b) 230 °C, (c) 250 °C, and (d) 270 °C.

A similar analysis was performed on all the BCPs, and the relevant T_A values are collected in Table 2. The occurrence of nanodomains with hexagonally packed cylinders, normally oriented with respect to the substrate, was observed for all the samples with the only exception of B29. For the latter sample, phase separation and perpendicular orientation of the cylinders occur but the lateral order is very low, as shown in Figure 3a,b, where the SEM images of sample B39 and B29 are compared.

The above results can be discussed within the frame of the mean-field phase diagram reported in Figure 3c. In the PS-*b*-PMMA system, the formation of a regular pattern occurs when the product χN (χ being the Flory−Huggins parameter and N the number of statistical segments per BCP chain) is higher than the minimum value that corresponds to the transition point from the ordered to the disordered state (ODT).[8,43] Pursuant to the phase diagram, no ordering can be achieved in lamellar forming symmetric BCPs with $\chi N < 10.5$ and in cylinder forming asymmetric BCPs having $\chi N < 15$. Although for PS-*b*-PMMA χ is only weakly temperature dependent, in the computation of the phase diagram, the χN values at the corresponding f were calculated for each M_n at the effective T_A. By superimposing the χN values obtained for the different BCPs on the phase diagram, we observe that, for all the samples except the B29 BCP, the χN values fall inside the area in which the cylindrical phase is expected to occur.

The χN value of the B29 ($\chi N = \sim 10.5$) with $f = 0.73$ lies well inside the zone of the phase diagram corresponding to the disordered phase. However, a clear evidence of phase separation with subsequent perpendicular orientation of the nanodomains was observed also for B29. This particular experimental behavior can be accounted for by considering that the phase diagram reported in Figure 3c was determined based on mean-field theory calculations for bulk materials, whereas the actual behavior of thin films should include the effect of the interfaces which in the present case seem to increase the propensity of the BCPs to segregate. Consequently, the reported phase diagram provides essentially a guideline for the interpretation of the results.

Characteristic Dimensions. Systematic SEM and GISAXS analyses were performed on all the samples exhibiting effective lateral organization to determine their morphological parame-

Table 2. Preparation and Morphological Parameters of Optimized BCP Samples: Film Thickness h (measured by ellipsometry), Annealing Temperature T_A, χN Values Calculated at $T = T_A$, Cylinder Diameter d (measured by SEM), Lattice Spacing Measured by SEM L_{0SEM} and by GISAXS $L_{0GISAXS}$, and Correlation Length ξ (measured by GISAXS)[a]

sample	h (nm)	T_A (°C)	χN (at T_A)	d (nm)	L_{0SEM} (nm)	$L_{0GISAXS}$ (nm)	h/L_0	ξ (nm)	ξ/L_0
B39	33	180	13.8	12.0 ± 2.0	24.0 ± 1.0	23.5 ± 0.2	1.37	447	19
B54	29	200	18.0	13.0 ± 1.0	28.8 ± 0.5	28.3 ± 0.3	1.00	477	17
B67	27	250	23.1	17.0 ± 1.0	35.0 ± 1.0	34.4 ± 0.4	0.77	710	21
B82	34	250	28.2	19.0 ± 2.0	42.9 ± 0.7	43.9 ± 0.7	0.79	535	12
B102	33	230	35.5	22.7 ± 1.5	47.0 ± 1.0	48.7 ± 0.9	0.70	434	9
B132	28	240	45.6	28.6 ± 1.6	59.0 ± 4.0	62.1 ± 1.4	0.47	354	6
B205	35	240	70.9	30.0 ± 4.0	73.0 ± 8.0	74.0 ± 2.0	0.48	357	5

[a]The value of L_0 used to calculate the ratios h/L_0 and ξ/L_0 are the ones obtained by SEM.

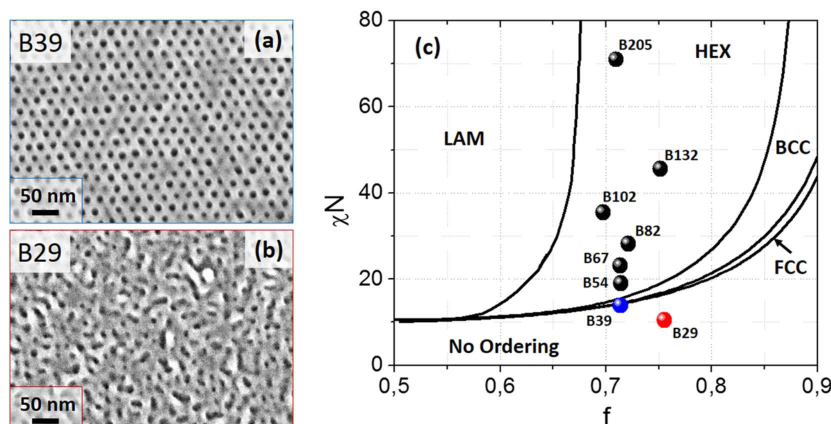

Figure 3. SEM images representing the morphology of the B39 (blue circle) and that of the B29 (red circle) are shown in (a) and (b), respectively. (c) Phase diagram of the BCP representing the χN product (calculated for the specific T_A, reported in Table 2) as a function of the styrene volume fraction f (adapted from Figure 2 in ref 8 with additional data). The black lines represent the phase boundaries of the lamellar phase (LAM), hexagonally packed cylindrical phase (HEX), spherical phase (BCC and FCC), and disorder phase. The circles correspond to the BCPs listed in Table 1.

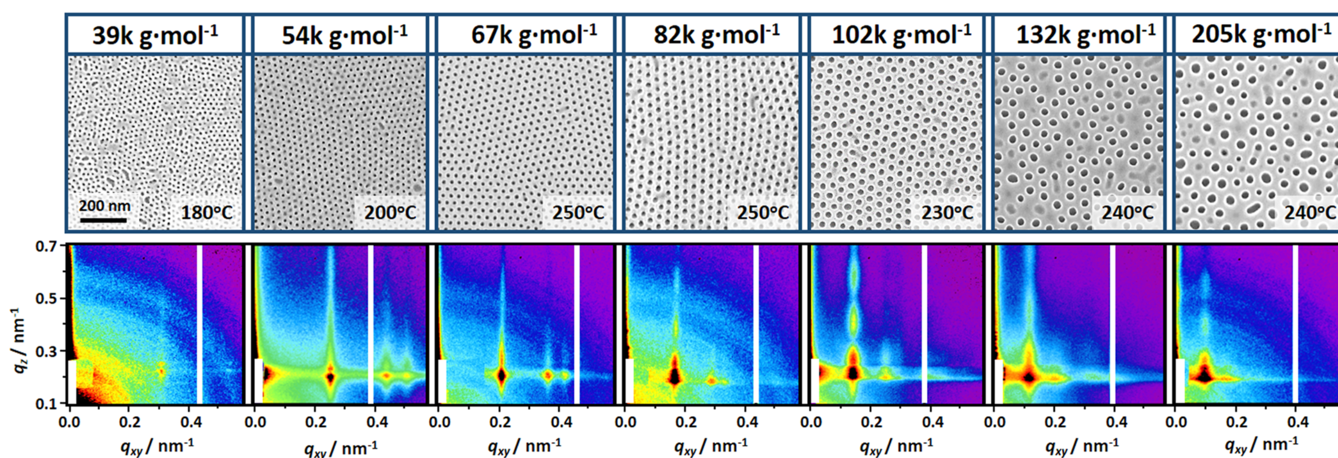

Figure 4. SEM images and corresponding GISAXS patterns for PS-*b*-PMMA thin films of increasing M_n after removal of PMMA domains. The corresponding annealing temperatures are also reported. All GISAXS patterns have been recorded at an incidence angle $\alpha_i = 0.18°$, except the B39 where $\alpha_i = 0.15°$. The white vertical line in the GISAXS patterns corresponds to the blind gap separating the active chips of the MAXIPIX detector.

ters. A collection of representative SEM images and corresponding GISAXS patterns is reported in Figure 4.

The SEM images show PMMA cylinders assembled to form a two-dimensional hexagonal lattice, with both the cylinder diameter d and the lattice constant L_0 progressively increasing with M_n. A close view of the different hexagonal patterns is provided in the left column of Figure 5 for all the BCP thin films.

The statystical analysis of the SEM images allows determining the values of d and L_0 with high accuracy. The histograms representing the statistical distribution of the PMMA cylinder diameters are reported in the right column of Figure 5: the dispersion in size of the PMMA cylinders is quite limited, apart from the B205 BCP. The broader dispersion of the cylinder size for this sample should be accounted for by considering both the higher polydispersity and the high molar mass which results in a very low chain mobility. The values of d, ranging from 12 ± 2 nm to 30 ± 4 nm, and L_0, from 24 ± 1 nm to 73 ± 8 nm, are reported in Table 2.

Contrary to what was observed in samples annealed in the furnace,[44] the RTP treatment affords perpendicular orientation of the PMMA cylinders irrespectively of the ratio h/L_0. Since h was nearly constant in the various samples, we obtained a different ratio h/L_0 for each M_n, with values varying from $h/L_0 \sim 4/3$ for sample B39 to $h/L_0 \sim 1/2$ for sample B205, as reported in Table 2. The perpendicular orientation was observed even in samples having $h/L_0 \sim 3/4$ (samples B82 and B102), in which the formation of half cylinders parallel to the substrate was observed to occur.[44]

The SEM morphological analysis was complemented by GISAXS investigation performed on all the samples. This technique allows exploring a much wider area than SEM (~10^6 times larger), providing additional information on the spatial extent of cylinder positional order and on its uniformity over the depth of the film.[45,46] Representative GISAXS patterns, taken above the critical angle ($\alpha_c \approx 0.14°$), are shown in Figure 4 below the corresponding SEM images. The quantities q_z and q_{xy} denote the components of the scattering vector normal and parallel to the plane of the sample, respectively. The presence of intensity rods, parallel to the q_z axis and set at discrete q_{xy} values, unequivocally indicates the in-plane periodicity of the PMMA domains and their orientation orthogonal to the plane of the film. The modulation of the rods along q_z, present in all the patterns though more visible in high M_n samples, is related

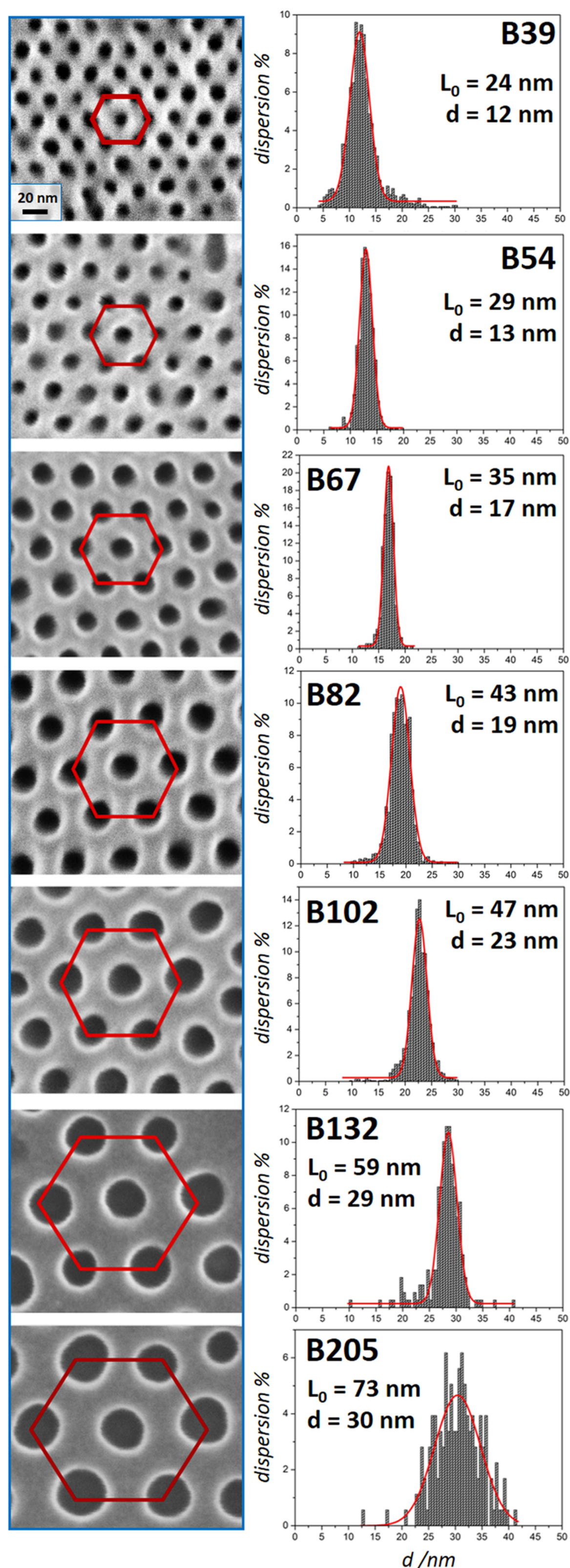

Figure 5. SEM images of the BCP thin films (left column) and the pore diameter distribution (on the right). The L_0 and d values indicated in the figure are rounded to the nearest integer. The exact values are reported in Table 2 with the corresponding error.

to the film thickness and provides values of h in agreement with those evaluated by ellipsometry and listed in Table 2.

Figure 6a shows the intensity profiles along q_{xy} obtained from horizontal cuts of the GISAXS patterns of Figure 4 at q_z = 0.22 nm^{-1} (sample B39) and q_z = 0.24 nm^{-1} (all other samples), i.e., on the maxima of scattered intensity. A series of peaks is visible, which can be indexed as the (h,k) reflections of a two-dimensional hexagonal lattice:

$$q_{h,k} = \frac{4\pi\sqrt{h^2 + hk + k^2}}{\sqrt{3L_0}}$$

Their shift towards lower q values is consistent with the anticipated increase of L_0 for higher M_n. In particular, the values of lattice spacing calculated from the q vector of the first order (1,0) reflection, $L_0 = 4\pi/\sqrt{3}q_{10}$, are in very good agreement with those obtained by SEM (see Table 2). Further measurements were carried out both above and below the critical angle, to probe the structural properties of the surface layer at different depths over the whole film thickness: at α_i = 0.12° the radiation penetration depth was calculated to be ~10 nm, i.e., one third of the film thickness h, whereas it was much larger than h for a_i = 0.15° and a_i = 0.18°. As shown in Figure 6b for the B54 sample, the comparison of the intensity profiles obtained from GISAXS patterns taken above and below the critical angle does not show significant differences in the peak position and width, thus suggesting that the film structure remains nearly uniform over the whole thickness of the sample. The presence of diffraction peaks at scattering vectors in the ratio $1:\sqrt{3}:\sqrt{4}:\sqrt{7}$ confirms the hexagonal arrangement of the PMMA cylinders, oriented normal to the substrate.

In Figure 7, the values of lattice spacing L_0 obtained both by SEM and GISAXS analyses are reported as a function of the number of segments N in the copolymer chain. The two sets of values are in excellent agreement within the experimental error and L_0 exhibits a clear exponential dependence on N, with $L_0 \propto N^{0.67}$. Theories about phase separation in polymeric blends or in BCPs identify three distinct regimes:[8] the weak segregation limit (WSL), in which $L_0 \propto N^{1/2}$, the strong segregation limit (SSL), in which $L_0 \propto N^{2/3}$, and the super strong segregation limit (SSSL), in which $L_0 \propto N^1$. The scaling exponent obtained from the fit of the data reported in Figure 7a indicates that the PS-*b*-PMMA system is in the SSL regime in the full range of the investigated molar masses, thus confirming and extending the results obtained by Xu et al.[24] for M_n > 73 kg·mol^{-1}.

From a technological point of view, the fine control of the characteristic dimensions (d, L_0) of the cylinder morphology provides the possibility to fabricate a periodic nanoporous pattern with tunable pore density. On the basis of the measured L_0 values we calculated the average pore density in the polymeric template for each BCP, reported in Figure 7b as a function of M_n. The calculated values range from 0.2 Td·inch^{-2} for sample B205 to 1.3 Td·inch^{-2} for sample B39, overcoming the 1 Td·inch^{-2} barrier and providing a viable route for nanostructure patterning in applications requiring very high density.[47]

The intensity profiles extracted from the GISAXS patterns and reported in Figure 6a exhibit significant differences in the number of diffraction peaks and in their width, with the samples of intermediate M_n showing narrower and, thus, better resolved diffraction peaks. Indeed, the width of the peaks provides a quantitative measure of the in-plane structural order. Within the Hosemann's paracrystalline model,[48] the order correlation length ξ can be calculated as

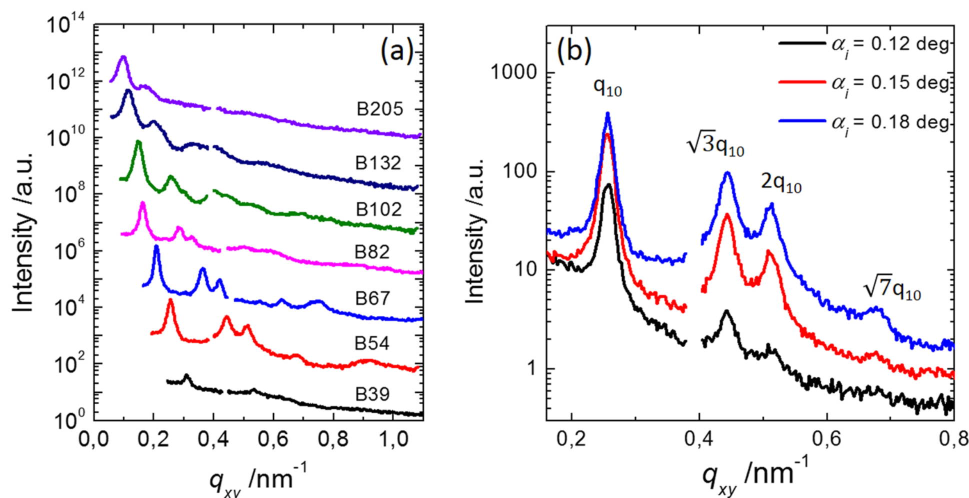

Figure 6. (a) GISAXS intensity profiles for samples with different M_n measured along q_{xy} at fixed q_z (q_z = 0.22 nm^{-1} for sample B39 and q_z = 0.24 nm^{-1} for all other samples). These data were extracted from the GISAXS patterns reported in Figure 4. (b) GISAXS intensity profiles of sample B54 measured at three different incidence angles, α_i = 0.12°, α_i = 0.15°, and α_i = 0.18°.

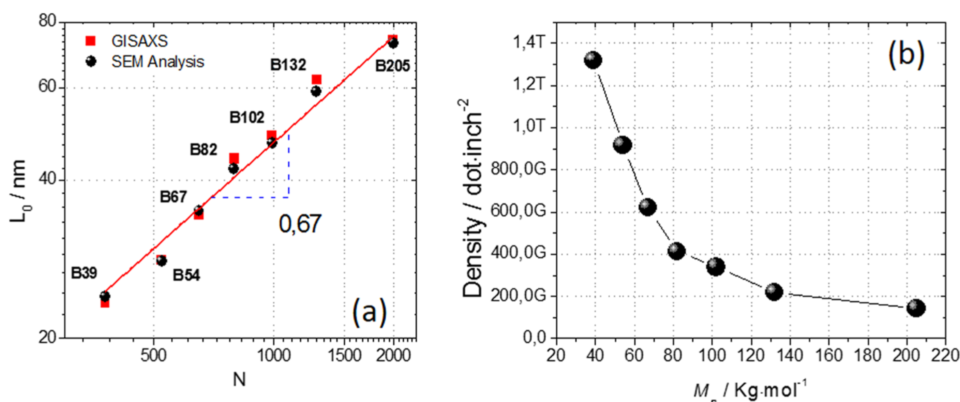

Figure 7. (a) Lattice spacing L_0 measured by SEM (black circles) and GISAXS (red squares) as a function of the number of segments N in the BCP. (b) Pore density as a function of the M_n.

$$\xi = \frac{2\pi^3}{6.25 \cdot \Delta q_{10}}$$

where Δq_{10} is the integral half-width of the first order (10) diffraction peak. This quantity gives a measure of the distance over which the long-range positional order is statistically lost. Applied to our data, this model provides the ξ values reported in Table 2: the highest correlation length (~700 nm) is obtained for sample B67, while the lowest (~300 nm) is for sample B132 and sample B205.

To better understand the meaning of these results, it can be useful to consider the trend of the ξ values expressed in units of the lattice spacing, i.e., through the fraction ξ/L_0 as a function of M_n (Figure 8). The histogram shows that for low M_n samples the in-plane order statistically extend over 18−20 consecutive lines of cylinders. With increasing M_n the fraction ξ/L_0 decreases, reaching the minimum value of five lattice spacings for sample B205. Such result suggests that for high M_n values the 900 s annealing time is not sufficient to obtain a good ordering of the nanodomains for the direct application in standard photolithographic processes. Nevertheless, to increase the lateral ordering of the nanostructures and the registration with the underlying substrate, methods such as chemically patterned substrates[49] and graphoepitaxy[50−52] have been widely explored in the literature. In the latter case, the nanodomains are laterally confined within lithographically defined trenches whose widths are commensurate with L_0, forming perfectly organized polymeric structures that propagate over long ranges. The extension of nanodomains obtained on flat substrates well correlate with the typical trench width (normally between 50 and 500 nm) exploited in the literature.[53,54]

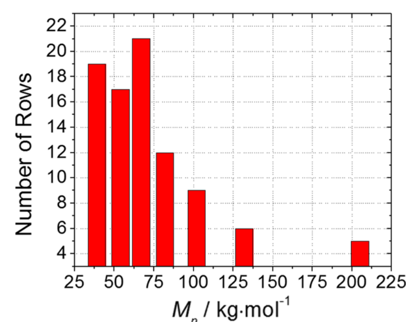

Figure 8. Histogram reporting the ratio ξ/L_0, expressed as number of rows, as a function of the BCP M_n.

CONCLUSIONS

In this work, the self-organization in PS-*b*-PMMA thin films undergoing a RTP treatment was investigated over a broad range of M_n between 29.4 kg·mol^{-1} and 205 kg·mol^{-1} as a function of the RTP annealing temperature. By optimizing this parameter for each M_n, we could get regular arrangements of hexagonally packed PMMA cylinders, embedded in a PS matrix and normally oriented with respect to the substrate, for all samples, except the B29 BCP. The hexagonally packed cylinder morphology, with d ranging between 12 and 30 nm and L_0 between 24 and 73 nm, was obtained in 900 s keeping the thickness of the polymeric film constant at ~30 nm. The lateral ordering of the nanostructures, measured by GISAXS, extended over a maximum of 20 consecutive rows of PMMA cylinders for the BCP having low M_n. These results demonstrate the possibility to control the self-assembly process of BCPs over a wide range of M_n values with a very simple and flexible thermal treatment. It represents an important step toward the simplification of the processing conditions required for the integration of these materials in a standard photolithographic process flow.

AUTHOR INFORMATION

Corresponding Author

*E-mail: michele.perego@mdm.imm.cnr.it.

Notes

The authors declare no competing financial interest.

ACKNOWLEDGMENTS

This research has been financially supported by the NANO-BLOCK project ("NANO-device fabrication using block copolymer based technology"). Patent protection related to this work is pending. The authors are grateful to Dr. T. Schulli, Dr. J. Hilhorst, Dr. C. Ferrero, ESRF, and Dr. I. F. Placentino, Università Politecnica delle Marche, for their valuable support.

REFERENCES

(1) Olson, D.; Chen, L.; Hillmyer, M. Templating Nanoporous Polymers with Ordered Block Copolymers. *Chem. Mater.* **2008**, *20*, 869−890.

(2) Yang, S. Y.; Ryu, I.; Kim, H. Y.; Kim, J. K.; Jang, S. K.; Russell, T. P. Nanoporous Membranes with Ultrahigh Selectivity and Flux for the Filtration of Viruses. *Adv. Mater.* **2006**, *18*, 709−712.

(3) Phillip, W. A.; O'Neill, B.; Rodwogin, M.; Hillmyer, M. A.; Cussler, E. L. Self-Assembled Block Copolymer Thin Films as Water Filtration Membranes. *ACS Appl. Mater. Interfaces* **2010**, *2*, 847−853.

(4) Segalman, R. A.; McCulloch, B.; Kirmayer, S.; Urban, J. J. Block Copolymers for Organic Optoelectronics. *Macromolecules* **2009**, *42*, 9205−9216.

(5) Joo, W.; Park, M. S.; Kim, J. K. Block Copolymer Film with Sponge-like Nanoporous Structure for Antireflection Coating. *Langmuir* **2006**, *22*, 7960−7963.

(6) Walheim, S.; Shaffer, E.; Mlynek, J.; Steiner, U. Nanophase-Separated Polymer Films as High-Performance Antireflection Coatings. *Science* **1999**, *283*, 520−522.

(7) Ruiz, R.; Kang, H.; Detcheverry, F. A.; Dobisz, E.; Kercher, D. S.; Albrecht, T. R.; de Pablo, J. J.; Nealey, P. F. Density Multiplication and Improved Lithography by Directed Block Copolymer Assembly. *Science* **2008**, *321*, 936−939.

(8) Koo, K.; Ahn, H.; Kim, S.-W.; Ryu, D. Y.; Russell, T. P. Directed Self-Assembly of Block Copolymers in the Extreme: Guiding Microdomains from the Small to the Large. *Soft Matter* **2013**, *9*, 9059.

(9) Park, M.; Harrison, C.; Chaikin, P. M.; Register, R. A.; Adamson, D. H. Block Copolymer Lithography: Periodic Arrays of ~10^{11} Holes in 1 Square Centimeter. *Science* **1997**, *276*, 1401−1404.

(10) Herr, D. J. C. Directed Block Copolymer Self-Assembly for Nanoelectronics Fabrication. *J. Mater. Res.* **2011**, *26*, 122−139.

(11) Sanders, D. P. Advances in Patterning Materials for 193 Nm Immersion Lithography. *Chem. Rev.* **2010**, *110*, 321−360.

(12) Bang, J.; Jeong, U.; Ryu, D. Y.; Russell, T. P.; Hawker, C. J. Block Copolymer Nanolithography: Translation of Molecular Level Control to Nanoscale Patterns. *Adv. Mater.* **2009**, *21*, 4769−4792.

(13) Du, P.; Li, M.; Douki, K.; Li, X.; Garcia, C. B. W.; Jain, a.; Smilgies, D.-M.; Fetters, L. J.; Gruner, S. M.; Wiesner, U.; Ober, C. K. Additive-Driven Phase-Selective Chemistry in Block Copolymer Thin Films: The Convergence of Top−Down and Bottom−Up Approaches. *Adv. Mater.* **2004**, *16*, 953−957.

(14) Kim, H.-C.; Park, S.-M.; Hinsberg, W. D. Block Copolymer Based Nanostructures: Materials, Processes, and Applications to Electronics. *Chem. Rev.* **2010**, *110*, 146−177.

(15) Lo, T.-Y.; Chao, C.-C.; Ho, R.-M.; Georgopanos, P.; Avgeropoulos, A.; Thomas, E. L. Phase Transitions of Polystyrene-b-Poly(dimethylsiloxane) in Solvents of Varying Selectivity. *Macromolecules* **2013**, *46*, 7513−7524.

(16) Black, C. T.; Ruiz, R.; Breyta, G.; Cheng, J. Y.; Colburn, M. E.; Guarini, K. W.; Zhang, Y.; Heights, Y. Polymer Self Assembly in Semiconductor Microelectronics. *IBM J. Res. Dev.* **2007**, *51*, 605−633.

(17) Fasolka, M. J.; Banerjee, P.; Mayes, A. M.; Pickett, G.; Balazs, A. C. Morphology of Ultrathin Supported Diblock Copolymer Films: Theory and Experiment. *Macromolecules* **2000**, *33*, 5702−5712.

(18) Metwalli, E.; Moulin, J.-F.; Rauscher, M.; Kaune, G.; Ruderer, M. A.; Van Bürck, U.; Haese-Seiller, M.; Kampmann, R.; Müller-Buschbaum, P. Structural Investigation of Thin Diblock Copolymer Films Using Time-of-Flight Grazing-Incidence Small-Angle Neutron Scattering. *J. Appl. Crystallogr.* **2010**, *44*, 84−92.

(19) Jeong, U.; Ryu, D. Y.; Kho, D. H.; Kim, J. K.; Goldbach, J. T.; Kim, D. H.; Russell, T. P. Enhancement in the Orientation of the Microdomain in Block Copolymer Thin Films upon the Addition of Homopolymer. *Adv. Mater.* **2004**, *16*, 533−536.

(20) Ham, S.; Shin, C.; Kim, E.; Ryu, D. Y.; Jeong, U.; Russell, T. P.; Hawker, C. J. Microdomain Orientation of PS-b-PMMA by Controlled Interfacial Interactions. *Macromolecules* **2008**, *41*, 6431−6437.

(21) Mansky, P.; Liu, Y.; Huang, E.; Russell, T. P.; Hawker, C. Controlling Polymer-Surface Interactions with Random Copolymer Brushes. *Science* **1997**, *275*, 1458−1460.

(22) Ryu, D. Y.; Ham, S.; Kim, E.; Jeong, U.; Hawker, C. J.; Russell, T. P. Cylindrical Microdomain Orientation of PS-b-PMMA on the Balanced Interfacial Interactions: Composition Effect of Block Copolymers. *Macromolecules* **2009**, *42*, 4902−4906.

(23) Han, E.; Stuen, K. O.; La, Y.-H.; Nealey, P. F.; Gopalan, P. Effect of Composition of Substrate-Modifying Random Copolymers on the Orientation of Symmetric and Asymmetric Diblock Copolymer Domains. *Macromolecules* **2008**, *41*, 9090−9097.

(24) Xu, T.; Kim, H.; Derouchey, J.; Seney, C.; Levesque, C.; Martin, P.; Stafford, C. M.; Russell, T. P. The Influence of Molecular Weight on Nanoporous Polymer Films. *Polymer* **2001**, *42*, 9091−9095.

(25) Böker, A.; Elbs, H.; Hansel, H.; Knoll, A.; Ludwigs, S.; Zettl, H.; Zvelindovsky, A. V.; Sevink, G. J. A.; Urban, V.; Abetz, V.; Muller, A. H. E.; Krausch, G. Electric Field Induced Alignment of Concentrated Block Copolymer Solutions. *Macromolecules* **2003**, *36*, 8078−8087.

(26) Kim, S. H.; Misner, M. J.; Xu, T.; Kimura, M.; Russell, T. P. Highly Oriented and Ordered Arrays from Block Copolymers via Solvent Evaporation. *Adv. Mater.* **2004**, *16*, 226−231.

(27) Metwalli, E.; Perlich, J.; Wang, W.; Diethert, A.; Roth, S. V.; Papadakis, C. M.; Müller-Buschbaum, P. Morphology of Semicrystalline Diblock Copolymer Thin Films upon Directional Solvent Vapor Flow. *Macromol. Chem. Phys.* **2010**, *211*, 2102−2108.

(28) Angelescu, D. E.; Waller, J. H.; Register, R. a.; Chaikin, P. M. Shear-Induced Alignment in Thin Films of Spherical Nanodomains. *Adv. Mater.* **2005**, *17*, 1878−1881.

(29) Zhang, X.; Harris, K. D.; Wu, N. L. Y.; Murphy, J. N.; Buriak, J. M. Fast Assembly of Ordered Block Microwave Annealing. *ACS Nano* **2010**, *4*, 7021−7029.
(30) Gotrik, K. W.; Ross, C. A. Solvothermal Annealing of Block Copolymer Thin Films. *Nano Lett.* **2013**, *13*, 5117−5122.
(31) Park, W. I.; Kim, K.; Jang, H.-I.; Jeong, J. W.; Kim, J. M.; Choi, J.; Park, J. H.; Jung, Y. S. Directed Self-Assembly with Sub-100 Degrees Celsius Processing Temperature, Sub-10 Nanometer Resolution, and Sub-1 Minute Assembly Time. *Small* **2012**, *8*, 3762−3768.
(32) Sinturel, C.; Vayer, M.; Morris, M.; Hillmyer, M. A. Solvent Vapor Annealing of Block Polymer Thin Films. *Macromolecules* **2013**, *46*, 5399−5415.
(33) Ferrarese Lupi, F.; Giammaria, T. J.; Ceresoli, M.; Seguini, G.; Sparnacci, K.; Antonioli, D.; Gianotti, V.; Laus, M.; Perego, M. Rapid Thermal Processing of Self-Assembling Block Copolymer Thin Films. *Nanotechnology* **2013**, *24*, 315601.
(34) Seguini, G.; Giammaria, T. J.; Ferrarese Lupi, F.; Sparnacci, K.; Antonioli, D.; Gianotti, V.; Vita, F.; Placentino, I. F.; Hilhorst, J.; Ferrero, C.; Francescangeli, O.; Laus, M.; Perego, M. Thermally Induced Self-Assembly of Cylindrical Nanodomains in Low Molecular Weight PS-B-PMMA Thin Films. *Nanotechnology* **2014**, *25*, 045301.
(35) Rasappa, S.; Borah, D.; Senthamaraikannan, R.; Faulkner, C. C.; Shaw, M. T.; Gleeson, P.; Holmes, J. D.; Morris, M. Block Copolymer Lithography: Feature Size Control and Extension by an over-Etch Technique. *Thin Solid Films* **2012**, *522*, 318−323.
(36) Borah, D.; Senthamaraikannan, R.; Rasappa, S.; Kosmala, B.; Holmes, J. D.; Morris, M. Swift Nanopattern Formation of PS-b-PMMA and PS-b-PDMS Block Copolymer Films Using a Microwave Assisted Technique. *ACS Nano* **2013**, *7*, 6583−6596.
(37) Busch, P.; Posselt, D.; Smilgies, D.; Rheinla, B.; Kremer, F.; Papadakis, C. M. Lamellar Diblock Copolymer Thin Films Investigated by Tapping Mode Atomic Force Microscopy: Molar-Mass Dependence of Surface Ordering. *Macromolecules* **2003**, 8717−8727.
(38) Black, C. T.; Guarini, K. W.; Breyta, G.; Colburn, M. C.; Ruiz, R.; Sandstrom, R. L.; Sikorski, E. M.; Zhang, Y. Highly Porous Silicon Membrane Fabrication Using Polymer Self-Assembly. *J. Vac. Sci. Technol. B* **2006**, *24*, 3188.
(39) Andreozzi, A.; Poliani, E.; Seguini, G.; Perego, M. The Effect of Random Copolymer on the Characteristic Dimensions of Cylinder-Forming PS-b-PMMA Thin Films. *Nanotechnology* **2011**, *22*, 185304.
(40) Ham, S.; Shin, C.; Kim, E.; Ryu, D. Y.; Jeong, U.; Russell, T. P.; Hawker, C. J. Microdomain Orientation of PS-b-PMMA by Controlled Interfacial Interactions. *Macromolecules* **2008**, *41*, 6431−6437.
(41) Gianotti, V.; Antonioli, D.; Sparnacci, K.; Laus, M.; Giammaria, T. J.; Ferrarese Lupi, F.; Seguini, G.; Perego, M. On the Thermal Stability of PS-b-PMMA Block and P(S-r-MMA) Random Copolymers for Nanopatterning Applications. *Macromolecules* **2013**, *46*, 8224−8234.
(42) Black, C. T.; Guarini, K. W. Structural Evolution of Cylindrical-Phase Diblock Copolymer Thin Films. *J. Polym. Sci., Part B: Polym. Phys.* **2003**, 1970−1975.
(43) Matsen, M. W.; Bates, F. S. Unifying Weak- and Strong-Segregation Block Copolymer Theories. *Macromolecules* **1996**, *29*, 1091−1098.
(44) Zucchi, I.; Poliani, E.; Perego, M. Microdomain Orientation Dependence on Thickness in Thin Films of Cylinder-Forming PS-B-PMMA. *Nanotechnology* **2010**, *21*, 185304.
(45) Daillant, J.; Quinn, K.; Gouriero, C.; Rieutordb, F. Grazing Incidence Surface Scattering of X-Rays. *J. Chem. Soc. Faraday Trans.* **1996**, *92*, 505−513.
(46) Lee, B.; Park, I.; Yoon, J.; Park, S.; Kim, J.; Kim, K.-W.; Chang, T.; Ree, M. Structural Analysis of Block Copolymer Thin Films with Grazing Incidence Small-Angle X-Ray Scattering. *Macromolecules* **2005**, *38*, 4311−4323.
(47) Yang, X.; Wan, L.; Xiao, S.; Xu, Y.; Weller, D. K. Directed Block Copolymer Assembly versus Electron Beam Lithography for Bit-Patterned Media with Areal Density of 1 Terabit/inch^2 and Beyond. *ACS Nano* **2009**, *3*, 1844−1858.
(48) Vainshtein, B. K. *Diffraction of X-Rays by Chain Molecules*; Elsevier: Amsterdam, 1966; Vol. *4*, p 227.
(49) Kim, S. O.; Solak, H. H.; Stoykovich, M. P.; Ferrier, N. J.; de Pablo, J. J.; Nealey, P. F. Epitaxial Self-Assembly of Block Copolymers on Lithographically Defined Nanopatterned Substrates. *Nature* **2003**, *424*, 411−414.
(50) Sundrani, D.; Darling, S. B.; Sibener, S. J. Guiding Polymers to Perfection: Macroscopic Alignment of Nanoscale Domains. *Nano Lett.* **2004**, *4*, 273−276.
(51) Cheng, J. Y.; Ross, C. A.; Smith, H. I.; Thomas, E. L. Templated Self-Assembly of Block Copolymers: Top-Down Helps Bottom-Up. *Adv. Mater.* **2006**, *18*, 2505−2521.
(52) Ferrarese Lupi, F.; Giammaria, T. J.; Seguini, G.; Laus, M.; Enrico, E.; De Leo, N.; Boarino, L.; Ober, C. K.; Perego, M. Thermally Induced Orientational Flipping of Cylindrical Phase Diblock Copolymers. *J. Mater. Chem. C* **2014**, *2*, 2175−2182.
(53) Han, E.; Kang, H.; Liu, C.-C.; Nealey, P. F.; Gopalan, P. Graphoepitaxial Assembly of Symmetric Block Copolymers on Weakly Preferential Substrates. *Adv. Mater.* **2010**, *22*, 4325−4329.
(54) Perego, M.; Andreozzi, A.; Vellei, A.; Ferrarese Lupi, F.; Seguini, G. Collective Behavior of Block Copolymer Thin Films within Periodic Topographical Structures. *Nanotechnology* **2013**, *24*, 245301.